Energetics of 2D and 3D Gold Nanoparticles on MgO(100): Influence of Particle Size and Defects on Gold Adsorption and Adhesion Energies

Stephanie L. Hemmingson, Gabriel M. Feeley, Naomi J. Miyake, and Charles T. Campbell*

Department of Chemistry, University of Washington, Campus Box 351700

Seattle, Washington 98189-1700 USA

Abstract

The adsorption of gold vapor onto MgO(100) films grown on Mo(100) was studied at 300 and 100 K using single crystal adsorption calorimetry (SCAC). The Au particle morphology was investigated using He^+ low-energy ion scattering spectroscopy (LEIS) and X-ray photoelectron spectroscopy (XPS). The LEIS data combined with particle shape measurements from the literature (Benedetti, S.; Myrach, P.; di Bona, A.; Valeri, S.; Nilius, N.; Freund, H.-J. *Phys. Rev. B* **2011**, *83* (12), 125423) reveal that, at both 300 K and 100 K, Au grows as 2D islands with bilayer thickness (~0.41 nm) up to a diameter of ~7 nm. At higher coverage, the islands thicken with little increase in diameter. The island densities are 3.0×10^{11} and 5.4×10^{11} per cm^2 at 300 K and 100 K, respectively. The initial sticking probability of Au is 0.90 at 300 K and 0.95 at 100 K. The surface residence time of the Au atoms that do not stick is <10 ms, implying that gold monomers bind to MgO(100) weakly (<69 kJ/mol). The adsorption energies indicate that Au particles of the same size bind more strongly to MgO(100) when grown at 300 K than at 100 K, which we attribute to Au binding to step edges or defects at 300 K, but at perfect MgO(100) terraces at 100 K (because Au diffusion is too slow to find defects). The adsorption energy of Au onto ~30-atom Au clusters is 285 kJ/mol at 300 K, ~68 kJ/mol higher than at 100 K, attributed to the difference between particles on defects versus terraces. Similarly, the adhesion energy of Au nanoparticles to MgO(100) extracted from the adsorption energies at 300 K is much higher (1.8 J/m^2 for ~7 nm particles at defects) than at 100 K (0.3 J/m^2 for ~7 nm particles at terraces). This 100 K adhesion energy is close to that estimated from electron-microscopy shape measurements of Au particles at terraces on MgO(100) (0.45-0.67 J/m^2). The heat of Au adsorption and Au chemical potential change by >100 kJ/mol as gold's 2D island size increases from 0.7 to 7 nm diameter, implying dramatic changes in catalytic activity and sintering rates with 2D diameter. This is the first experimental measurement of any metal adsorption energy on any oxide as a function of island diameter when making 2D islands, as well as the first direct comparison of any adhesion energy found from calorimetric adsorption energies to that from particle shape analysis.

* Corresponding author: charliec@uw.edu Phone: (206) 616-6085

Keywords: gold, nanoparticle catalysis, metal adsorption, oxide support, metal/support interaction, adhesion energy, heat of adsorption.

1.Introduction

Supported gold nanoparticles have attracted significant attention in the last decade as potential catalysts for CO oxidation, selective oxidations, and other industrially-relevant reactions, as well as in the fields of photonics, plasmonics, nanotechnology, and biology.[1–3] Despite the fact that gold is inert in its bulk form, gold nanoparticles between 1 and 6 nm in size are catalytically active for a variety of different reactions.[4–7] For example, gold nanoclusters dispersed across high surface area metal oxide supports have shown great potential as low temperature CO oxidation catalysts.[6,8–11] The catalytic properties of such oxide-supported gold nanoparticles depend strongly on both the size of the nanoparticles and the properties of the oxide (surface structure and orientation, reducible or non-reducible, defect concentration, etc.). Significant strides towards understanding the origin of these effects have been made by studying well-defined model systems in ultrahigh vacuum conditions,[12–14] with Au nanoparticles on MgO(100) being one of the most intensively studied model catalysts.[15–31] Here we report calorimetric measurements of the adsorption energies of Au atoms as they nucleate and grow nanoparticles on MgO(100), and extract from these the Au / MgO(100) adhesion energies and particle size dependence of the Au atom chemical potential. We also use surface-sensitive spectroscopy to study Au growth morphology, and report for the first time the chemical potential of Au atoms in Au nanoparticles on MgO(100) as a function of particle size. We also report here the first ever measurements of the heat of adsorption of any metal atom in making 2D islands and their chemical potential as a function of 2D island size (from 0.7 to 7 nm diameter, or 10 to 2000 atoms). We have previously shown that the chemical potential of the metal atoms in supported metal nanoparticles correlates with the reactivity of their surface metal atoms:[32] the higher their chemical potential, the more strongly they bind small adsorbed catalytic reaction intermediate. As their chemical potential increases, the metal atom becomes less noble, behaving more like metals that reside farther to the left in the periodic table. Also, the higher their chemical potential is, the larger is the thermodynamic driving force for them to sinter, and the faster they deactivate by sintering during extended use as catalysts.[32–34] Thus, this surprisingly large change in chemical potential as the 2D island diameter increases from 0.7 to 7 nm (~100 kJ/mol) implies that catalytic activity and sintering rates change dramatically with 2D island diameter even when the gold particles maintain the same bilayer thickness. This is an important step toward clarifying the dramatic effect of particle size on activity and selectivity in gold oxidation catalysis. We also explore the effects of defect sites on these energies, using temperature to control the location of those nanoparticles at terrace versus defect sites.

Among the oxide surfaces studied in model catalysts, MgO(100) is one of the most prevalent. MgO is a simple stoichiometric binary oxide with a rocksalt structure and well-defined surfaces that are stable under most catalytic operating conditions. The most stable (001) surface has only minor structural differences from the bulk,[35] has very poor electron transfer properties, and can be prepared readily by cleavage,[36,37] by the production of MgO smoke,[29,38] or by thin film growth.[39–44] However, despite several decades of attention, much remains unclear about this insulating oxide surface. Specifically, it has been observed that defects are critical contributors to the physical and chemical properties of MgO, and play a dominant role in the adsorption behavior of its surfaces (an excellent review of the complexity and significance of these defects is presented in ref [35]). For example, while bulk MgO does not absorb or emit light between 200 and 900 nm, luminescence bands have been observed in MgO smoke[38,45,46], MgO powders[47,48] and in defect-poor MgO(100) films[49] at energies that are significantly lower than the bandgap, which Benedetti *et al.*[49] assigned to under-coordinated corner sites (3-fold) and step edges (4-fold). While a defect free MgO(100) surface does not interact with CO[50,51] or CO_2,[52] MgO powders are highly reactive to CO.[53] The nature and the identification of these defects, as well as their effects on adsorption and catalytic properties, is still under debate.

For several decades, the primary defect of interest was the surface oxygen vacancy or F-center, which can contain localized electrons[54,55] and can be produced on MgO(100) by electron bombardment.[49] Au is known to nucleate preferentially on F centers in MgO(100),[20,25,56,57] and it has been predicted by theory[1,57–61] and confirmed by experiment[26] that F-centers can transfer electronic charge to supported metal nanoparticles. UHV experiments showed that 8-atom Au clusters deposited on defect-free MgO(100) supports were essentially inert, while Au clusters of this same size were active towards CO oxidation on highly defective MgO(100) films.[1,61] Furthermore, shifts in CO FTIR[62] indicate that small Au clusters bound to electron-rich defects form negatively charged species. For decades this evidence pointed to oxygen vacancies as the primary activators of supported metal nanoparticles, which contributed to the belief that F-centers are present in relatively high concentrations on the surface of as-prepared MgO(100) samples. However, recent results show that the number of F-centers on MgO surfaces is very low unless they are specifically treated to create them, and these vacancy defects alone cannot explain many of the observed features in MgO reactivity.[35]

Possible candidates to replace the F-center model are four-coordinated Mg and O ions located at steps or edges, or the defects formed by the intersection of two MgO steps perpendicular to each other, known as a reverse corner.[63,64] Au particles have been shown to preferentially nucleate at step edges over terraces on MgO(100) at 300 K and above[23,28,36,37,65,66] and experimental evidence suggests that these morphological defects in MgO(100) films can also act as strong electron traps.[35,64] Additionally, hydroxyl groups on the oxide surface may act as sites for bound electrons, and hydroxylated MgO(100) surfaces have been shown to oxidize Au particles[67] and enhance the stability of Au clusters against thermal sintering.[68] While UHV conditions minimize the concentration of such impurities on the surface, traces of even a small concentration of water may decorate the oxide steps with OH groups.

When MgO(100) films are grown on Mo(100), as we do here, STM shows that the mismatch between Mo and MgO causes a Moire pattern to form when films are less than ~5 ML thick.[49] Above this thickness, the dominant defects are step edges and screw dislocations that align into a dislocation network. These electron-rich dislocation defects persist until thicknesses of over 10 ML, however STM imaging above 15 ML is difficult due to the decreasing conductivity of the films.[49] The MgO(100) films prepared in this investigation are thick enough (~3.5 nm) that it is reasonable to assume that step edges are the most common type of defect present, however dislocations and line defects may still be present in small quantities. Additionally, the preparation conditions ensure a negligible concentration of F-centers and surface hydroxyls, which is confirmed by the absence of spectroscopic signal due to such species. However, because Au has such a high electronegativity, it is likely that a small concentration of morphological defects affects the measured calorimetric binding strength of Au, as well as the morphology of Au particles that are vapor-deposited onto MgO(100) films, which cannot be prepared completely free of all defects. For this reason, the experiments presented here are conducted on highly-ordered, ~3.5 nm thick, defect-poor MgO(100) films at both 300 K and 100 K. At lower temperatures, Au atoms diffuse more slowly, which increases the probability that Au particles will nucleate at less favorable terrace MgO(100) sites rather than steps or edges. This allows for a direct experimental comparison of the adsorption and adhesion energies, as well as the morphology, of Au particles adsorbed at terraces versus defect sites. In a short report, we already presented the adhesion energy measured here at terrace sites and compared it to other metal-on-oxide adhesion energies.[69]

2. Experimental

A detailed description of the adsorption microcalorimetry apparatus and experimental procedure is presented elsewhere.[70] The calorimeter operates in a UHV chamber with a typical base pressure below ~1 x 10^{-10} Torr. The apparatus is also equipped with low energy electron diffraction (LEED), Auger electron spectroscopy (AES), X-ray photoelectron spectroscopy (XPS), low energy ion scattering spectroscopy (LEIS), a quadrupole mass spectrometer (QMS), and two quartz crystal microbalances (QCM). Surface spectroscopy signals are obtained with a PHI 10-360 precision energy analyzer equipped with a PHI 72-250 position sensitive detector. LEIS measurements are carried out using He^+ ions with 1.5 keV primary energy from a focused ion beam that is rastered rapidly over an area of 2 mm x 2 mm. XPS measurements are performed with an Al Kα source that operates at 12 kV and 200 W.

The calorimeter consists of a pulsed metal atom beam and a pyroelectric polymer (polyvinylidenefluoride, PVDF) heat detector that is pressed into the back of a 1 μm thick single crystal Mo(100) sample, which is ~8 mm in diameter. The MgO(100) films studied here were grown in the vacuum chamber on the front-face of this Mo(100) sample, as described below. A 4-mm diameter, collimated and chopped Au atom beam is generated using an electron-beam evaporator. This results in a spatially and temporally well-defined 100 ms pulse that contains ~0.02 ML of Au dosed every two seconds onto the front face of the sample. Au coverage is given throughout in ML, where 1 ML is equal to the surface atomic density of oxygen in the MgO(100) surface (1.12 x 10^{15} atoms/cm^2). The Au was purchased from Kurt J Lesker with

99.99% purity. A transient temperature change in the ribbon results in a measurable change in its face-to-face voltage whose magnitude is proportional to the heat released upon metal adsorption. The detector response was calibrated before and after experiment using pulses of known energy from a HeNe laser. However, it was difficult to directly measure both the initial optical reflectivity of the oxide-coated metal sample, which changes slightly from run to run due to differences in oxide film thickness, as well as the final reflectivity after Au deposition, which similarly varies slightly with final Au thickness due to the high degree of surface roughness. Therefore, the absolute calibration factor in each run was estimated by using the initial reflectivity at a single oxide thickness, and then performing the same laser calibration measurements on the sample both before and after Au deposition, assuming that the change in the sample reflectivity was the only parameter that changes the magnitude of the detector response to the laser. The calibration factor thus obtained was then corrected slightly so that the multilayer heat of adsorption in the high-coverage limit would equal to the literature value for the bulk heat of sublimation of bulk Au(solid) at 300 K and 100 K.[71] To convert the calorimetrically measured internal energy changes into standard enthalpy changes at the sample temperature (300 K or 100 K), the excess translational energy of the Au gas atoms at the oven temperature above that for a Maxwell-Boltzmann distribution at the surface temperature was subtracted, and a small pressure-volume work term (RT per mole) was added, as described elsewhere.[72,73]

The absolute flux of Au atoms in each pulse was measured using a calibrated QCM that translates into the sample position (along the central axis of the atomic beam) before and after each calorimetry experiment. A second off-axis QCM monitors the flux of metal atoms during the entire duration of the experiment. It has been shown previously[70] that the ratio between the flux measured at these two QCMs changes linearly with time within the duration of our experiment. Therefore, by measuring the initial and final flux ratios between these two QCMs, the flux at the monitor QCM can be scaled to provide the flux at the sample position during heat measurements. The sticking probability was measured using a modified King-Wells method,[74] using a line-of-sight QMS to measure the fraction of Au atoms that transiently adsorb to the surface but do not stick permanently. This QMS signal is compared to a reference zero sticking pulse from a hot Ta flag (1800-2000 K), which is located at the same position as the sample and corrected for average velocity. Since these Au atoms are produced from a hot source that is line-of-sight to the detector, the fraction of the heat signal due to optical radiation must be subtracted from the total signal. This contribution is measured by translating a BaF_2 flag into the beam path prior to and following calorimetry, which blocks all of the metal atoms, but transmits a known fraction of the radiation.

The sample and heat detector are held in contact with a thermal reservoir during calorimetry, which can be cooled by liquid nitrogen. The temperature is monitored by two type K thermocouples attached to the sample holder and to the PVDF ribbon holder near the sample. Before each calorimetry measurement, the detector was retracted and the surface was flash-heated to 700 K (measured by optical pyrometry) in 1×10^{-6} Torr O_2 to remove any adsorbed background gases. See references [70,72,75] for more details of these procedures.

The growth morphology of Au on MgO(100) was determined using LEIS and XPS with a 135 degree scattering angle. LEIS was conducted using a 2×10^{-7} torr He background and 3 mA emission current which gives an ion current of ~90 nA/cm^2 averaged over the rastered area. The sample is mounted onto a manipulator fork that can be cooled to 100 K by a liquid nitrogen reservoir for transfer between the calorimetry position and the analysis position. The temperature of the manipulator fork was monitored by a type K thermocouple spot-welded near the sample.

The MgO(100) thin films were grown on Mo(100) in an adjacent UHV preparation chamber. The Mo(100) surface was cleaned by thermal annealing to 1600 °C in UHV for 1-2 minutes until no C was present in XPS and a sharp Mo(100) LEED pattern was observed. Because the Mo(100) films were very thin, excessive heating risked damage to the crystals (creating small holes and tears), and therefore very small quantities of O were sometimes still observable on the Mo(100) by XPS after this annealing treatment. This small amount of O did not measurably affect either the Mo(100) or the MgO(100) LEED quality, the XPS spectra of the grown MgO(100) films, or the calorimetric results. The MgO(100) films were grown via reactive evaporation of Mg (Kurt J. Lesker, 99.95%), first in UHV at 25 °C for 1 minute, and then in a 1×10^{-6} torr O_2 background gas at a sample temperature of 300 °C. The as-grown films were then annealed at 550 °C in this same background pressure of oxygen for 2 minutes to ensure a minimal concentration of oxygen vacancies.

3. Results

3.1 MgO(100) thin film characterization.

Thin films of MgO(100) were grown in a connected UHV chamber to a thickness of 3.5 ± 0.7 nm (~13-20 MgO(100) layers) on a 1 µm thick Mo(100) substrate as described above. This thickness was obtained by depositing Mg onto Mo(100) at 300 °C in 1 x 10^{-6} Torr O_2 for four minutes while maintaining a constant QMS signal for Mg (m/e = 24), and then measuring the attenuation of the Mo $3p_{3/2}$ peak with XPS to give the MgO(100) film thickness, and thus the deposition rate. The average MgO deposition rate was 0.1 nm/min as determined by the attenuation of the Mo $3p_{3/2}$ photoelectron peak, using the inelastic mean free path of Mo $3p_{3/2}$ electrons escaping through MgO calculated using NIST inelastic mean free path database (25.7 Å). Once this rate was determined, MgO(100) films were grown at the same conditions while maintaining this constant QMS signal magnitude (i.e., Mg flux) for the amount of time needed for the desired 3.5 nm thickness. The (100) surface order was verified by LEED, which gave a sharp (1 x 1) square pattern. The one-to-one ratio of Mg to O was confirmed by comparing the relative magnitudes of the Mg 2s and O 1s signals, corrected for atomic sensitivity factor and instrument response function. No carbon, metallic Mg, or other elements were observed in XPS. All the films were annealed at 700 °C in O_2 for two minutes after initial growth, however this annealing did not affect the quality of the LEED or the XPS spectrum.

MgO(100) films grow epitaxially with their (001) planes parallel to Mo(001) and the MgO(100) direction aligned with Mo(110), which is due to the 5% lattice mismatch between body-centered cubic Mo (a = 3.15 Å) and rocksalt MgO (a = 2.98 Å).[49] We have shown previously for the case of $CeO_2(111)$ that oxide films thicknesses greater than 2 nm produce bulk-like adsorption properties.[76] However, in the case of MgO(100) films, it has been observed that larger thicknesses (>15 layers, i.e., >3.1 nm) are required to produce flat, defect-poor films.[49,77] When our films were thinner than 13 layers (~2.7 nm), the observed LEED spots were substantially more diffuse than the ~3.5 nm-thick films used below.

3.2 Au sticking probability on MgO(100) at 300 K and 100 K.

The sticking probability of Au atoms onto MgO(100) as a function of total Au coverage was measured by monitoring the number of non-sticking Au atoms in each pulse. This sticking probability was determined as previously[72] by comparing the magnitude of the time-integrated transient QMS signal for Au vapor during each calorimetry pulse to a zero-sticking reference signal that was generated by placing a hot Ta foil flag in the sample position and resistively heating it so all of the incoming Au atoms rapidly desorb. The fraction of atoms that did not stick was then used to scale the absorbed heat per pulse in kJ/mol and the cumulative total Au coverage. The sticking probabilities versus coverage for both 300 K and 100 K are shown in Figure 1.

At 300 K, the sticking probability starts high at 90%, as we would expect for metals with large bulk cohesive energies, and then increases to unit sticking probability, which it approaches (to within 1%) at ~2 ML. At 100 K, the sticking probability starts higher, at 95%, and reaches unity more rapidly (by ~1.5 ML). Measured sticking probabilities that are above 90% is consistent with what we have found for other late transition metals (Cu and Ag) on MgO(100).[78]

3.3 Au particle and film morphology on MgO(100) observed with LEIS and XPS.

The Au nanoparticle morphology on MgO(100) at 300 K and 100 K was tracked with He^+ LEIS as shown in Figure 2(a). Discreet quantities of Au were deposited using similar dose rates as those used during calorimetry. The attenuation of the Mg and O LEIS substrate signals and the growth of the Au adsorbate signal were monitored as a function of total Au coverage. The integrated Mg and O LEIS peak areas were normalized to the signals from the clean MgO(100) film prior to Au deposition. We typically normalize the integrated Au peak areas to a high-coverage point where no substrate signal is visible, however even at very high Au coverages (>50 ML), the Mg and O LEIS peaks were still visible, and this was repeatable across multiple runs. The integrated areas of these substrate peaks were typically ~15-30% of the initial clean Mg and O signals at both 300 K and 100 K (though routinely less at 100 K), and the two values were always within ~2% of each other. Therefore, to represent the signal for a bulk-like continuous Au overlayer, the final highest-coverage integrated Au peak area was scaled by $(1 - S/S_0)$, where S/S_0 is the average of the remaining Mg and O signals relative to their initial values. This scaled Au signal was used to normalize the Au LEIS peaks.

To ensure that no significant ion damage was done to the sample by He^+ ion bombardment during the LEIS experiments in Figure 2(a), control experiments were done in each case using only four coverage points: 0 ML, 0.6 ML, 3 ML, and >60 ML. The zero and "full" coverage points are used for normalization, and the two intermediate points were chosen at signals that are still highly sensitive to small changes in coverage. This procedure resulted in four-fold less total ion beam exposure at those points, yet the data from these experiments fell within error of the data in Figure 2(a). This indicates that He^+ ion beam damage did not significantly affect these results.

From 0-0.4 ML, the integrated Au LEIS signals increase nearly linearly with a slope of approximately 1/2 at both 300 K and 100 K. Above this coverage, the Au signal increases much more gradually with coverage. This behavior of the Au LEIS signals is mirrored by the Mg and O signals at both temperatures, which decrease with the same trend. The normalized Au LEIS peaks at 100 K are always slightly larger than the normalized signal at 300 K, and similarly the Mg and O normalized LEIS signals at 100 K are always slightly smaller than those at 300 K.

Since LEIS is sensitive only to the topmost atomic layer, the normalized overlayer and substrate signals represent a nearly direct measurement of the fraction of the oxide surface that is masked and unmasked, respectively, by adsorbed nanoparticles.[79] From this, we see that only ~35-40% of the surface is covered by Au at 6 ML.

If Au was growing on MgO(100) in a layer-by-layer fashion, the normalized Au LEIS signal would increase linearly with a slope of one (reaching 100% of the surface covered by 1 ML). We do observe a linear change in signal from 0-0.4 ML, but the slope of 1/2 suggests that Au is growing as 2D islands with bilayer thickness in this region. The “roll over” that occurs at ~0.4 ML suggests that the morphology of Au films above this coverage is different than this bilayer-island morphology, in that the thickness is quickly increasing, as in 3D nanoparticles.

When 2D or 3D metal particles grow during vapor deposition on oxide surfaces, it is generally observed that after a nucleation stage (which only requires a few percent of a monolayer to complete), the number density of particles reaches a saturation value, and thereafter does not change substantially until the particles start to become so big that they overlap and fuse.[80–82] Indeed, even while the particle *shape* is changing, it has been observed with TEM[65,83] and AFM[28] that when Au is vapor-deposited onto bulk-like MgO(100) crystals that the particle *density* first rapidly increases (nucleation) and then remains constant (growth) over a large coverage range until the Au particles become large enough to coalesce. This has similarly been observed with STM for Au that is deposited onto thin films of MgO(100) grown on Mo(100), where the particle density similarly remains nearly constant (within a factor of two) until the coalescence regime is reached.[25] We will therefore assume constant number density of Au particles in analyzing our LEIS data here from the lowest Au coverage studied up to a coverage where ~35% of the surface is covered by Au.

The morphology of 3D metal nanoparticles grown on oxide surfaces is often modeled with the hemispherical cap model, which assumes that the nanoparticles grow with a hemispherical shape and constant particle density, changing in size only.[84,85] Since the normalized LEIS signals directly measure the fractional coverage, the normalized Au signal can be modeled as:

$$I / I_0 = f_s = n\,(A_{\text{particle,int}} + A_{\text{shadowed}}) \qquad (1)$$

where n is the particle density in particles/cm^2, $A_{\text{particle,int}}$ is the interfacial area per particle, and A_{shadowed} is the additional footprint area of the substrate that is shadowed from the incident ion beam or detector by the particle.[85] This equation is valid when the particles all have the same size and shape. For the shape of hemispherical caps in our LEIS analysis geometry where the incident ion beam is parallel to the surface normal and angle of detection is 45 degrees from the surface normal, this equation becomes:

$$f_s = 1.207 n \pi R^2 \qquad (2)$$

where R is the hemispherical particle radius.[85]

However, as we show below, these LEIS data are not fit well by the hemispherical cap model at all coverages with any single particle density. Therefore, in order to model the LEIS data, we turn to published STM data for evidence of the particle shape. Benedetti *et. al.*[21] observed that Au particles grown on 2-2.5 nm thick MgO(100) films at 300 K had flat-topped triangular and hexagonal shapes in the region from 0-5 ML Au coverage, typically oriented with one of their three or six edges aligned with a MgO(110) direction. These Au particles had the lowest aspect ratio of all metals studied on MgO(100),[21] defined as the ratio of particle's maximum height to the longest interfacial axis. This aspect ratio was not constant over the entire coverage range studied by STM, which explains the failure of the hemispherical cap model here, as it requires that the particle shape remain constant.

We next determine the Au particle density based on the LEIS data at a single coverage where the geometry of the system is known (by using the STM observations of a similar system, such as those measured by Benedetti *et. al.*[21] described above). By assuming that this particle density remains constant with coverage, we then interpret the LEIS data at other coverages in terms of both particle shape and size.

At 2 ML Au coverage on MgO(100) at 300 K, Benedetti *et. al.*[21] observed with STM that the flat-topped Au nanoparticles have different orientations and an average aspect ratio of 0.3.

We make the simplification that an array of flat-topped triangular and hexagonal shapes with different orientations can be roughly described as averaging out to a collection of flat circular disks, so that the shadowed area does not depend on particle's orientation. With a 45-degree detection angle, the shadowed area is just the diameter of the disk multiplied by its thickness, which is directly related to the aspect ratio. For the observed aspect ratio a of 0.3 at 2 ML, we obtain:

$$I / I_0 = f_s = n\ (\pi R^2 + 1.2R^2) = n\pi R^2\ (1+1.2\pi) = 1.382 n\pi R^2 \tag{3}$$

This equation for modeling the LEIS data is functionally identical to that for hemispheres above, but with a slightly larger prefactor of 1.382 instead of 1.207 due to more macroscopic shadowing. The value of R at any given coverage can be determined by the total amount of Au deposited d expressed as the average Au thickness (i.e., d = the Au coverage in atoms per unit area times the volume per atom in bulk Au(solid)), given by:

$$d = nV_{\text{particle}} = n\pi R^2(t) = n\pi R^2(2aR) = 2na\pi R^3 \tag{4}$$

where V_{particle} is the volume per disk-shaped particle. At ~2 ML where $a = 0.3$ and $d = 0.38$ nm, this gives $R = 1.26n^{-1/3}$. Substituting this into Equation (3) above and using $I / I_0 = 0.215$ from the LEIS measurement at 2 ML at 300 K gives a particle density of $n = 3.0 \times 10^{11}$ particles/cm^2. (Here we combined Au, Mg, and O normalized LEIS data to best estimate I / I_0.). Assuming the same particle shape at 2 ML and 100 K as observed by STM at 2 ML and 300 K (above) gives a number density of 5.2×10^{11} particles/cm^2 at 100 K. The higher density at 100 K is consistent with the general trend that particle densities are higher at lower temperatures.[80,81,86–88] By comparison, if we were to instead assume hemispherical shapes at this same coverage, the particle density that best fits the 2 ML data is 5.5×10^{11} particles/cm^2 at 300 K, and 1.0×10^{12} particles/cm^2 at 100 K. It should be noted that these n values are slightly larger due to the effects of assumed shape on both the shadowing factor and the relationship of R to the volume per particle.

We can replot the LEIS data to show the average Au particle thickness as a function of total Au deposited. By dividing this average film thickness d at each coverage by the fractional area covered by Au particles as measured by LEIS (using the Au, Mg, or O normalized signal, modified by the macroscopic shadowing factor), we obtain the average Au particle thickness, similar to previous reports.[88,89] Although this requires an assumption of a macroscopic shadowing factor which depends on particle shape, which we have established is likely changing, this dependence is weak enough that a reasonable approximation can be made by assuming that it is constant at the value for an aspect ratio of 0.3 (i.e., 1.382, see above). Figure 2(b) shows the data in Figure 2(a) replotted in this way as the average Au particle thickness versus coverage at both 300 K and 100 K. Additionally, the lines indicate the thickness that would be expected from the disk-model with a fixed aspect ratio of 0.3 assuming the same particle density found in Figure 2(a).

As seen in Figure 2(b), at low coverage the Au particles are thicker than single-layers (indicated by the dashed line), but significantly thinner than the fixed-aspect-ratio model predicts. On the other end above 2 ML, the particles are much thicker than the model suggests. In other words, their aspect ratio is initially lower than 0.3, and then increases well above this value, suggesting that the particles are growing thicker far faster than they are growing laterally across the surface. We reanalyze these data below without any assumption about the macroscopic shadowing factor and obtain similar results, with these conclusions even more obvious.

Since the particle densities remain constant with coverage at both 300 K and 100 K (at the values found above at 2 ML), and the Au particles have flat tops according to STM (see above), we will assume that they remain approximately disk-shaped, and estimate their aspect ratio *a* and effective radius *R* at every coverage. These parameters are related through the total thickness of Au film, *d,* given by Equation (4) and the fractional area masked in LEIS by the gold particles, f_s, is given by the number density of particles times the surface area of the top-face of the disk plus the extra area of the substrate that is shadowed from the detector by the disk at the detection angle of 45° from normal:

$$f_s = n(\pi R^2 + 4aR^2) \tag{5}$$

These two relationships provide a system of two equations with two unknowns, *a* and *R*, for each coverage. The diameters and aspect ratios that result from this analysis are shown in Figures 3(a) and 3(b).

As seen at both 300 K and 100 K, the aspect ratio of the particles increases as the total Au deposition increases, reaching approximately 0.5 (the aspect ratio of hemispheres) by ~3.6 ML. Further supporting our analysis above, the data from ~3.6 ML to ~5.5 ML can be reasonably well fit with the hemispherical cap model with particle densities of 3.4×10^{11} particles/cm^2 at 300 K and 5.4×10^{11} particles/cm^2 at 100 K, which are extremely similar to the values found at 2 ML for flat disks. From 0-1 ML, the aspect ratio ranges from ~0.1 to 0.2, which is consistent with the findings of Benedetti *et. al.*[21] The aspect ratio appears to be nearly the same for both 300 K and 100 K across the entire coverage range, however this could be due to the aforementioned assumption that they are the same at 2 ML.

The particles' effective diameter (Figure 3(a)) increases very rapidly from 0 to 0.4 ML, but then levels off to remain essentially constant to ~5 ML, with an average value of ~7 nm above 0.4 ML (using points at both 100 K and 300 K). This would indicate that the Au particles reach some critical lateral size (effective diameter) of 7 nm by 0.4 ML, and continue to grow mainly in thickness but very little in diameter at higher coverages, consistent with the increase in aspect ratio. Close inspection of Figure 3(a) reveals that the diameter appears to increase very slowly between 0.4 to ~5.5 ML at 300 K, from ~7 to ~8 nm. At 100 K there is no measurable increase outside the noise from the slightly lower average diameter of ~6.5 nm above 0.4 ML.

Finally, knowing a and R allows us to more precisely determine the thickness of the disks *without* any assumption of macroscopic shadowing area (given by $2aR$ per particle above). Using this relationship, the data in Figure 2(b) have been replotted in 3(c). While the general trend is similar to what we observed in Figure 2(b), the early-coverage points are even lower in thickness, and the high-coverage points are even higher. Additionally, the thicknesses at very low coverages (from 0-0.4 ML) average 0.45 ± 0.09 nm, which is within error equal to the thickness of two Au(100) atomic layers (0.407 nm). We choose Au(100) layers rather than Au(111) here because this epitaxial relationship has been observed on MgO(100) and predicted by multiple groups,[16,19,23,36,90,91] although some have also observed Au growth with the (111) orientation,[49] or a disordered Au structure that can rapidly change shape, as in quasi-melting.[66] The horizontal grey line in Figure 3(c) indicates this bilayer thickness. This agrees with our observation in the normalized LEIS data of Au particles potentially growing as 2D islands with bilayer thickness.

The morphology of Au on MgO at 300 K was also monitored with XPS using the integrated normalized intensities of the Au $4f_{5/2}$, Mg 1s, Mg 2p, and O 1s signals as a function of Au coverage. The Mg 2p and Au 4f peaks were deconvoluted using the procedure described in reference [92]. XPS is far less surface-sensitive than LEIS, and is therefore not as sensitive to changes in particle shape. It was used here only to verify general agreement. The data below 0.4 ML were well-described by a single-layer growth model for XPS (XPS is not sensitive enough to distinguish between single-atom thick layers and bilayers), and above that coverage the data were fit well by both a flat disk model with 3.0 x 10^{11} particles / cm^2 and a hemispherical cap model with a particle density of 3.5 x 10^{11} particles / cm^2.

3.4 Heat of Adsorption at 300 K and 100 K

The calorimetric heats of Au atom adsorption on MgO(100) at 300 K and 100 K are shown as a function of total Au coverage in ML in Figure 4. These adsorption heats have been adjusted for the sticking probability of Au, to get the heat *per mole adsorbed*, as described above, as well as for the small translational energy difference between atoms emitted from the hot metal atom source and these same atoms in a Boltzmann distribution at the sample temperature (either 300 K or 100 K), as described previously.[72] With this correction, these data correspond to the standard molar enthalpy of adsorption with both the gas and the solid at the temperature of the MgO(100) film (multiplied by negative one, so that exothermic values are presented as positive rather than negative, as is conventional in calorimetry).

At 300 K and 100 K, the initial heat of adsorption of Au on MgO(100) is 285 kJ/mol and 209 kJ/mol, respectively. As Au coverage increases, the heat of adsorption first increases rapidly, but then slowly levels off, reaching within 10 kJ/mol of the bulk heat of sublimation of Au(solid) (368 kJ/mol at 300 K, 363 kJ/mol at 100 K[71]) by ~2 ML for both temperatures. The lower value of initial heat at 100 K compared to 300 K is likely due to a higher fraction of Au atoms adsorbing to terrace sites rather than stronger-binding step and corner sites that are accessible at 300 K, due to slower Au adatom diffusion at 100 K (see Discussion). Most late transition metals that are vapor-deposited on oxides bind preferentially at steps and kink sites / corners when the temperature is high enough for the adatoms to diffuse to the steps,[80,81,93] and this was found to be the case for Au on MgO(100) in both DFT calculations[17,94] and experiments at temperatures above 300 K.[23,28,36,37,65,66]

The lineshape of the Au mass spectrometer signal versus time for the atoms that did not stick was analyzed at both 300 K and 100 K. It was found to be indistinguishable from the line shape generated by the Au atoms that desorb during zero-sticking measurements, which essentially measures the instrument response function of the mass spectrometer signal versus time as the beam pulse ends. This indicates that the incoming Au atoms that adsorb onto MgO(100) but do not stick must have an average surface residence time, τ, that is <10 ms, which is the time resolution of this measurement. We will assume that these Au atoms which did not stick permanently were indeed transiently adsorbed as monomers. This assumption is supported by the fact that the Au atoms in atomic beams striking NaCl(100) and KBr(100) surfaces at 644 K and 555 K leave the surface in cosine angular distributions,[95] and thus are nearly 100% accommodated to those surfaces even at those much higher temperatures. The fact that τ is <10 ms here means that the removal rate constant for Au monomers adsorbed on MgO(100), $k_{\text{total}} = 1/\tau$, is $>100\ \text{s}^{-1}$. These adsorbed monomers are removed by two processes: sticking permanently to Au clusters, and desorbing. If we assume both these processes have rates that are 1st order in Au monomer concentration, with rate constants k_{stick} and k_{des}, respectively, then $k_{\text{total}} = k_{\text{stick}} + k_{\text{des}}$, and the sticking probability S must be: $S = k_{\text{stick}}/(k_{\text{stick}} + k_{\text{des}})$. (The sticking rate is only first-order after the saturation density of clusters is reached, but that occurs already after the first pulse or two.) Combining these relations gives that $k_{\text{des}} = k_{\text{total}}(1-S)$, so that $k_{\text{des}} > 100\ \text{s}^{-1}(1-0.90) > 10\ \text{s}^{-1}$ at 300 K and $k_{\text{des}} > 100\ \text{s}^{-1}(1-0.95) > 5\ \text{s}^{-1}$ at 100 K. By assuming a prefactor for the desorption rate constant ($k_{\text{des}} = \nu \exp(-E_{\text{des}}/RT)$ of $\nu = 10^{13}\ \text{s}^{-1}$, this lower limit on the rate constant implies that the desorption activation energy for Au monomers on MgO(100) must therefore be below 69 kJ/mol at 300 K, and below 24 kJ/mol at 100 K. These are substantially smaller than the initial heats of adsorption on Figure 4 of 285 and 209 kJ/mol at 300 K and 100 K, respectively.

4. Discussion

4.1 Comparison to DFT calculations for Au monomers

DFT calculations predict Au monomer adsorption energies onto the regular terrace sites of MgO(100) ranging from 52-96 kJ/mol[17,94,96–100] (where the Au atom is positioned on top of an oxygen anion, which has been confirmed experimentally to be the preferred terrace binding site for Au adatoms[101]). The upper limit on the Au monomer's surface residence time measured above set an upper limit on the desorption activation energy for Au monomers on MgO(100) of <69 kJ/mol at 300 K, and <24 kJ/mol at 100 K. While the value at 300 K falls within the range of DFT adsorption energies, the value at 100 K is significantly lower. The value at 100 K of <24 kJ/mol is consistent with the 300 K limit of <69 kJ/mol, only more restrictive. This 100 K limit of <24 kJ/mol is more likely to represent Au binding at terrace sites, since they might diffuse to sample defects at 300 K. Del Vitto *et. al.*[94] calculated a 40% (36 kJ/mol) larger binding energy for an Au monomer on a MgO(100) step compared to on top of a terrace oxygen.

4.2 Comparing morphology to previous studies

The LEIS results of Figure 3(c) indicate bilayer island growth in the first 0.4 ML. Blick *et. al.*[24] saw two-dimensional Au rafts in TEM images of Au/MgO powder catalysts formed by wet impregnation. These rafts were the dominant form of Au at low loadings. In simulations of cluster geometry on the MgO(100) surface using many-body potentials based on first principle calculations, Ferrando *et. al.*[19] found that for 30-atom clusters, FCC(001) bilayers are nearly degenerate with the global minimum shape of square pyramids. Even if 2D islands are not thermodynamically preferred, their growth could occur due to kinetic effects.[80,102] Recently, it was predicted first by DFT[103] and then confirmed by experiment[104] that when MgO(100) films grown on Ag(100) are thinner than 8 layers (~1.6 nm), Au grows exclusively as 2D islands. Certainly however, this last example is likely the effect of an interaction between Au and the underlying substrate, which our MgO(100) films are thick enough to eliminate since they are ~3.5 nm thick.

The growth of 2D metal islands at low coverage was also reported in our previous work for Cu[105] and Ag[106] on MgO(100), where the normalized AES signals were fit well by a layer-by-layer growth model below 0.3 ML. Since AES is far less sensitive than LEIS, those measurements were likely unable to distinguish between monolayer and bilayer islands in this regime.

Given the strong initial heats of adsorption measured here and the formation of large-diameter 2D bilayer islands, it is surprising that the O and Mg LEIS signals are still strong in LEIS at very high Au coverages (>60 ML). In contrast, in our group's experiments for Ag on MgO(100), the O signal in AES was no longer visible above 30 ML Ag coverage,[106] despite the larger probe depth of AES compared to LEIS. This supports our observation that once a critical two-dimensional diameter of ~7 nm has been reached, the Au particles exclusively thicken at nearly fixed diameter (Figure 3(a)), getting very thick (up to ~4-5 nm) but never entirely covering the MgO(100) substrate. Once again, this may occur because the binding of single Au monomers to MgO(100) terraces is so weak that they diffuse readily to find a nearby large Au particle, where their binding is apparently preferred when they step-up onto the topmost plane. Del Vitto *et. al.*[94] calculated a very low value for the single Au atom diffusion barrier on the MgO(100) surface of ~0.2 eV, and Metois *et. al.*[107] observed extremely mobile Au adatoms on cleaved MgO(100) surface at 300 K. Such a growth model where islands thicken without getting wider can occur for kinetic reasons,[102] but it may also occur due to the buildup of strain with increasing island size due to lattice mismatch.[108,109]

4.3 Variation of the heat of Au adsorption with Au nanoparticle size

We next replot the calorimetric data versus the geometric parameters of the particles formed, such as thickness and effective diameter. To get a continuous relationship between thickness t and coverage (Θ), the data at both 300 K and 100 K in Figure 3(c) were fit to a modified exponential of the form $t = A(1 - \mathrm{EXP}(-B\Theta))^{C}$, as shown by the dashed lines in red and blue for 300 K and 100 K, respectively.

The heat versus coverage data of Figure 4 are replotted versus the resulting thickness in Figure 5. The thicknesses for the first 10 to 20 data points of the heat curves in Figure 4 fall below the thickness of one Au(100) atomic layer (0.203 nm), which is un-physical. Therefore, we forced the early coverage points to equal the thickness of two Au(100) layers based on the LEIS evidence that Au is forming bilayers. The heat increases with thickness, approaching within 10 kJ/mol of the bulk heat of sublimation by a thickness 3.2 nm.

In the low-coverage range, these data represent the heat of adsorption of Au when adding to 2D Au bilayer islands at constant thickness such that the 2D islands are changing only in their effective diameter. We estimated their average diameter at each coverage here by first determining the average number of atoms in each particle (based on the coverage and the best-fit particle density), and then by assuming these particles have the density of bulk Au(solid) and the thickness of a Au(100) bilayer in bulk Au(solid) (i.e., 0.406 nm). The Au heat of adsorption versus the resulting 2D Au island diameter in this constant bilayer thickness regime is shown in the inset of Figure 5. On the top axis of this inset is also shown the average number of atoms per particle, which is proportional to the square of the diameter. This is the first time the heat of adsorption has ever been measured as a function of 2D particle diameter for any metal on any oxide surface.

The data in Figure 5 present the *differential* heats of adsorption as a function of particle size, which directly reflect differences in the chemical potential of the metal atoms, but with opposite sign, as described in references [86] and [32]. In brief, entropic contributions to the free energy are small compared to the large changes in enthalpy measured here, so we neglect these entropic contributions, and the chemical potential of a metal atom in particles of diameter D, μ(D), relative to that of the bulk metal, μ(∞), (set as the reference zero here) is just the heat of sublimation of bulk Au minus the differential heat of Au adsorption at diameter D. Thus, another way to view the data from Figure 5 is to plot the chemical potential versus average effective particle diameter (or particle thickness), which is shown on the right-hand axes of Figure 5. When evaluated in this way, we see that 1 nm diameter bilayer Au islands are ~160 kJ/mol higher in chemical potential that those that have reached the bulk size limit (>7 nm in diameter and >2.5 nm thick). Additionally, Au atoms in 1.5 nm diameter 2D islands at 100 K are ∼65 kJ/mol higher in chemical potential than 1.5 nm diameter 2D islands at 300 K (due to the difference in Au particles nucleated at defects at 300 K versus terraces at 100 K, see below).

The surprisingly large change in chemical potential with 2D island size alone at 100 K (~100 kJ/mol, Fig. 5 inset) implies that catalytic activity and sintering rates of Au nanoparticle catalysts change dramatically with 2D island diameter, since both measures of catalytic performance are known to depend strongly on chemical potential[106]. The strong increase in chemical potential with decreasing 2D size seen here reflects the thermodynamic driving force for catalysts to sinter into larger particles with time on stream, leading to dramatic increases in sintering rates with increasing chemical potential.[86,32,34] It also shows why it is challenging to maintain gold nanoparticles at their small size, and reflects a decreasing propensity for the metal to bind strongly to small adsorbates.[32]

Finally, the heat of adsorption and corresponding chemical potential of Au atoms in Au particles versus the number of atoms per particle is shown (as determined above) over a larger coverage range without an assumption of particle geometry at 300 K and 100 K in Figure 6. These two datasets converge at particle sizes above ~1400 atoms. Interestingly, Ferrando *et. al.*[19] calculated that above 1200 atoms, Au particles cross over from FCC(001) geometry to the Au bulk-preferred FCC(111). The convergence in the heat data suggests that once particles reach this size, they are spread across such a large area of the MgO(100) surface that the incoming adatoms that attach to the particle no longer feel any significant energetic difference between attachment to a particle nucleated on a terrace and one at a defect. This seems to coincide well with the point at which these nanoparticles are beginning to reach a size that resembles their stable bulk properties.

4.4 The effect of temperature on adsorption energy: the role of defects

We proposed previously that the heat data at 100 K includes more contributions from Au binding at terrace sites than the heat at 300 K. To examine this, we compare the heat of adsorption of Au on MgO(100) at 300 K to that at 100 K for the smallest common particle size that we are able to measure. At 300 K, the initial Au heat of adsorption (285 kJ/mol) corresponds to Au particles that contain ~31 atoms. In contrast, the heat of adsorption of Au at the same particle size of 31 atoms at 100 K is only 217 kJ/mol, 68 kJ/mol lower than at 300 K. This large difference in the temperature-dependent adsorption energies on MgO(100) can only arise if these Au particles are at different sites. The fact that the adsorption energies are so dramatically lower at 100 K – where there is less thermal energy for Au atom diffusion –indicates that these measurements at 100 K are due to Au particles at weak-binding terraces, while at 300 K they are from Au particles that were thermally able to nucleate at the stronger-binding defects, which was enabled by the faster diffusion of Au particles at 300 K.

4.5 Adhesion Energy of Au on MgO(100)

The adhesion energy of nanoparticles onto a flat surface, E_{adhesion}, can be found from the integral heat of adsorption and the morphology measured in LEIS using a thermodynamic cycle described in reference [80]. This gives the following relationship:

$$n\cdot\sum_{n}\Delta H_{\text{adsorption}} = -n\cdot\Delta H_{\text{sublimation}} + A\cdot[(1+f)\gamma_{\text{v/m}} - E_{\text{adhesion}}] \qquad (7)$$

where $\gamma_{\text{v/m}}$ is the surface free energy of the bulk nanoparticle material, f is the surface roughness factor, $\sum_{n}\Delta H_{\text{adsorption}}$ is the integral molar heat of adsorption up to the coverage of interest, n is the number of moles of the adsorbate on the surface at that coverage, A is the total area covered by the metal, and $\Delta H_{\text{sublimation}}$ is the bulk heat of sublimation of the adsorbate.

For particles, we typically apply this method to the large-particle limit, which is the highest coverage where no more than ~35% of the surface is covered by the adsorbate (as determined by LEIS).[106] (At higher coverages, particles may start to overlap, after which their size can no longer be estimated.) For Au on MgO(100), the normalized LEIS signals do not reach this point until ~5.5 ML, which is in the region where these particles have become approximately hemispherical. This method also requires us to know the surface roughness factor at the point where adhesion is determined. When the Au particle geometry is changing at any given coverage, the roughness factor changes with it. For instance, for a continuous, atomically-smooth adsorbate layer, the roughness factor is 1; for hemispherical caps it is 2; and for flat disks with $a = 0.3$ (as seen with STM at 2 ML[49]), the roughness factor is 2.2.

At 300 K, if we use the integrated heat at 2 ML along with measured particle density of 3.0×10^{11} particles/cm^2 assuming flat disks with this same STM aspect ratio (i.e., $a = 0.3$, for which $f = 2.2$), the resulting adhesion energy is 2.24 J/m^2. These disk-shaped particles are ~8.1 nm in diameter and ~2.4 nm thick at this coverage according to this model. If the value of Au / MgO(100) adhesion is lower than the Au / Au adhesion energy -- which is simply twice the Au surface free energy -- this indicates that Au favors forming 3D clusters rather than wetting the surface. Using the value of 1.51 J/m^2 for the Au(111) surface free energy,[110] assuming that once these Au particles reach this size, they adopt their preferred 111 interface, then the Au / Au adhesion energy is 3.02 J/m^2. This value is indeed larger than the range of Au / MgO(100) adhesion energies measured here at 300 K, consistent with our observation of the formation of 3D particles at high coverages. The formation of 2D bilayer islands at low coverage thus seems to be due to a kinetic limitation in this case, rather than a thermodynamic preference, since the heats of Au adsorption measured here at low coverage are far lower than on large 3D particles. Kinetically-driven 2D growth is common,[80,102] and has been observed for Ag on MgO(100).[111]

An important role of defects on the adhesion energy can be seen by comparing this adhesion energy at 300 K to the corresponding value at 100 K, where defects are less populated due to slower metal monomer diffusion.[28,80–82,93,112] By using the same coverage region (up to 2 ML) and roughness factor discussed above at 300 K, a similar analysis of the calorimetry data at 100 K gives an adhesion energy of 0.31 J/m^2 at 100 K for 6.7 nm diameter disk-shaped particles. To compare particles of similar size, the adhesion energy of ~7 nm particles at 300 K (assuming the same shape and aspect ratio as the value 2 ML coverage found above for 8.1 nm particles), is 1.81 J/m^2, which is nearly6-fold larger. Combined with the evidence presented above for particle-size dependent adsorption energies that depend on temperature, these very different adhesion energies at 300 K and 100 K further confirm that at 100 K, we are measuring the adsorption and adhesion energies of Au particles on the terraces of MgO(100), while at 300 K we are measuring the adsorption and adhesion energies of Au particles at defects. While we cannot directly visualize the binding sites of Au particles using calorimetry, the combined spectroscopic and calorimetric results presented here are strong evidence that we have measured information about the binding strength of large Au particles at defects at 300 K and on terraces at 100 K.

The calorimetric adhesion energy of ~7 nm diameter disk-shaped Au particles on MgO(100) measured here at 300 K (1.81 J/m^2) is much higher than the values determined at 300 K using TEM particle-shape measurements for 2-6 nm diameter Au particles of on MgO(100), which was only 0.45-0.67 J/m^2.[29,32,113] However, the calorimetric adhesion energy of 0.31 J/m^2 at 100 K for ~7 nm diameter disk-shaped particles agrees *far* better with these values determined from TEM particle shapes. Importantly, in these TEM measurements, the Au particles that were analyzed appear to be at terraces with no morphological defects present.[29,113] Thus, it makes sense that the 100 K calorimetry value, which is also at terraces, should agree better with these TEM measurements at terraces than the 300 K calorimetry value, which we attribute to particles at defect sites instead (probably step edges). These lower values found with TEM at 300 K and by calorimetry at 100 K also agree significantly better with DFT calculations of the adhesion energy of 1-2 layers of Au on MgO(100) terraces (0.16-0.42 J/m^2).[57]

We next rule out other possible reasons why the calorimetric adhesion energy for Au on MgO(100) at 300 K is so much larger than that at 100 K and from TEM particle-shape analysis (for particles on terraces at 300 K). The calorimetric values were measured here on MgO(100) films that ranged from 2 to 5 nm thick, which was thick enough to reach the bulk-thickness limit for Ag on $CeO_2(111)$.[76] Therefore, it is unlikely that they were affected by significant interaction from the underlying Mo(100) substrate. Furthermore, our oxidizing preparation conditions make it highly unlikely that we have enough oxygen vacancies to affect the heats, also supported by the absence of vacancy-related signal in the XPS spectra. This is important, because oxygen vacancies bind Au adatom 210-300 kJ/mol more strongly than terrace sites on MgO(100).[20,57,58,94,97] The only reasonable explanation for the difference in our adhesion energy at 300 K relative to that at 100 K or from TEM is the role of step edges or other surface morphological defects on our calorimetric adhesion energy here at 300 K.

This is the first ever direct comparison between adhesion energies measured with calorimetry and this same quantity measured using a different technique (TEM). While the value measured by calorimetry at 300 K differs greatly from that measured by TEM at 300 K, the disagreement is due to the effect of step edges on the calorimetric value at 300 K. Indeed, the value measured by calorimetry at 100 K for Au particles on terraces agrees well with that measured by TEM at 300 K, also for Au particles on MgO(100) terraces. Our calorimetric measurements reveal that the energy of Au nanoparticles on MgO(100) is highly sensitive to morphological defects such as steps, corners, and kinks, where they bind much more strongly than at terraces. Recently, morphological defects such as the "reverse corner" have been proposed to explain the electron-transfer properties of MgO(100) films that had previously been attributed to oxygen vacancy defects.[63,64] The thermodynamic cost to form an oxygen vacancy on an MgO(100) terrace is extremely high (5-10 eV),[114–116] and in most cases they are not present in large enough concentrations to effect observed results. In contrast, morphological defects, as well as those with higher dimensionality such as grain boundaries, have been observed experimentally in much higher concentrations. These defects can act as efficient electrostatic traps in thick MgO films, and Au has been observed to nucleate on these defects and grain boundaries.[62] Since Au is characterized by its high electronegativity, the very strong binding we see for Au at these types of defects may be due to their electron-rich character.

5. Conclusions

The heat of Au adsorption onto MgO(100) versus Au island diameter is measured here for coverages below 0.4 ML, where the Au grows as flat 2D islands of bilayer thickness. This is the first time the heat of adsorption has ever been measured as a function of 2D particle diameter for any metal on any surface. Intensities in LEIS versus coverage showed that at both 300 K and 100 K, Au grows on MgO(100) first as 2D bilayer islands up to ~0.4 ML coverage, where their diameter grows with coverage until an average diameter of ~7 nm at 300 and 100 K. At ~0.4 ML, these islands suddenly stop growing in diameter, and instead thicken with coverage. Using details of the Au particle shape and aspect ratio found at 2 ML Au coverage in the STM work of Benedetti *et al*[21] at 300 K, the Au particle density was determined to be 3.0×10^{11} particles/cm^2 at 300 K, and slightly larger (5.2×10^{11}) at 100 K due to slower adatom diffusion. At 300 K, the Au heat of adsorption for particles containing 31 atoms is 285 kJ/mol, while at 100 K it is 68 kJ/mol lower, indicating that the measurements at 100 K are from Au particles at weak-binding terraces, while at 300 K they are from Au particles that nucleate at stronger-binding defects. An analysis of the lineshape of the Au mass spectrometer signal for nonsticking atoms provides an upper limit for the desorption activation energy for Au monomers on MgO(100) of 69 kJ/mol at 300 K, and 24 kJ/mol at 100 K. The adhesion energy of Au particles on MgO(100) at 2 ML Au coverage was determined using the particle shape and roughness factor described by Benedetti *et. al.*[21] At 300 K this value for ~7 nm particles is 1.81 J/m^2, while at 100 K it is 0.31 J/m^2. The value at 100 K agrees far better with adhesion energy measurements found on this system using particle shape techniques, which supports the conclusion that the adhesion energy at 100 K is for Au particles nucleated on MgO(100) terraces, while the much larger value at 300 K is due to particles at step edges and kinks, or other defects.

6. Acknowledgements

The authors acknowledge the Department of Energy, Office of Basic Energy Sciences, Chemical Sciences Division Grant No. DE-FG02-96ER14630 for support of this work.

7. References

(1) Sanchez, A.; Abbet, S.; Heiz, U.; Schneider, W.-D.; Häkkinen, H.; Barnett, R. N.; Landman, U. *J. Phys. Chem. A* **1999**, *103* (48), 9573–9578.

(2) Gong, J. *Chem. Rev.* **2012**, *112* (5), 2987–3054.

(3) Daniel, M.-C.; Astruc, D. *Chem. Rev.* **2004**, *104* (1), 293–346.

(4) Haruta, M. *Chem. Rec.* **2003**, *3* (2), 75–87.

(5) Haruta, M. *Catal. Today* **1997**, *36* (1), 153–166.

(6) Haruta, M. *CATTECH* **2002**, *6* (3), 102–115.

(7) Valden, M.; Lai, X.; Goodman, D. W. *Science* **1998**, *281* (5383), 1647–1650.

(8) Haruta, M.; Yamada, N.; Kobayashi, T.; Iijima, S. *J. Catal.* **1989**, *115* (2), 301–309.

(9) Meyer, R.; Lemire, C.; Shaikhutdinov, S.; Freund, H. *Gold Bull.* **2004**, *37* (1–2), 72–124.

(10) Haruta, M.; Kobayashi, T.; Sano, H.; Yamada, N. *Chem. Lett.* **1987**, *16* (2), 405–408.

(11) Bond, G. C.; Thompson, D. T. *Gold Bull.* **2000**, *33* (2), 41–50.

(12) Goodman, D. W. *Chem. Rev.* **1995**, *95* (3), 523–536.

(13) Goodman, D. W. *Surf. Rev. Lett.* **1995**, *2* (1), 9–24.

(14) Bäumer, M.; Freund, H.-J. *Prog. Surf. Sci.* **1999**, *61* (7–8), 127–198.

(15) Molina, L. M.; Hammer, B. *Phys. Rev. B - Condens. Matter Mater. Phys.* **2004**, *69* (15), 1–22.

(16) Pauwels, B.; Van Tendeloo, G.; Bouwen, W.; Theil Kuhn, L.; Lievens, P.; Lei, H.; Hou, M. *Phys. Rev. B - Condens. Matter Mater. Phys.* **2000**, *62* (15), 10383–10393.

(17) Fuente, S. A.; Ferullo, R. M.; Domancich, N. F.; Castellani, N. J. *Surf. Sci.* **2011**, *605* (1–2), 81–88.

(18) Li, Z.; Ciobanu, C. V; Hu, J.; Palomares-Báez, J.-P.; Rodríguez-López, J.-L.; Richards, R. *Phys. Chem. Chem. Phys.* **2011**, *13* (7), 2582–2589.

(19) Ferrando, R.; Rossi, G.; Levi, A. C.; Kuntová, Z.; Nita, F.; Jelea, A.; Mottet, C.; Barcaro, G.; Fortunelli, A.; Goniakowski, J. *J. Chem. Phys.* **2009**, *130* (17), 174702.

(20) Frondelius, P.; Häkkinen, H.; Honkala, K. *New J. Phys.* **2007**, *9* (9), 339–339.

(21) Benedetti, S.; Myrach, P.; di Bona, A.; Valeri, S.; Nilius, N.; Freund, H.-J. *Phys. Rev. B* **2011**, *83* (12), 125423.

(22) Yulikov, M.; Sterrer, M.; Risse, T.; Freund, H.-J. *Surf. Sci.* **2009**, *603* (10–12), 1622–1628.

(23) Cowley, J. M.; Neumann, K. D. *Surf. Sci.* **1984**, *145* (2–3), 301–312.

(24) Blick, K.; Mitrelias, T. D.; Hargreaves, J. S. J.; Hutchings, G. J.; Joyner Richard, W.; Kiely, C. J.; Wagner, F. E. *Catal. Letters* **1998**, *50* (3), 211–218.

(25) Benia, H. M.; Lin, X.; Gao, H. J.; Nilius, N.; Freund, H. J. *J. Phys. Chem. C* **2007**, *111*, 10528–10533.

(26) Sterrer, M.; Yulikov, M.; Fischbach, E.; Heyde, M.; Rust, H.-P.; Pacchioni, G.; Risse, T.; Freund, H.-J. *Angew. Chemie Int. Ed.* **2006**, *45* (16), 2630–2632.

(27) Risse, T.; Shaikhutdinov, S.; Nilius, N.; Sterrer, M.; Freund, H.-J. *Acc. Chem. Res.* **2008**, *41* (8), 949–956.

(28) Højrup-Hansen, K.; Ferrero, S.; Henry, C. R. *Appl. Surf. Sci.* **2004**, *226*, 167–172.

(29) Giorgio, S.; Chapon, C.; Henry, C. R.; Nihoul, G.; Penisson, J. M. *Philos. Mag. A* **1991**, *64* (1), 87–96.

(30) Molina, L. M.; Hammer, B. *Phys. Rev. Lett.* **2003**, *90* (20), 206102.

(31) Zhang, C.; Yoon, B.; Landman, U. *J. Am. Chem. Soc.* **2007**, *129* (8), 2228–2229.

(32) Campbell, C. T.; Sellers, J. R. V. *Faraday Discuss.* **2013**, *162*, 9–30.

(33) Campbell, C. T. *Acc. Chem. Res.* **2013**, *46* (8), 1712–1719.

(34) Farmer, J. A.; Campbell, C. T. *Science* **2010**, *329* (5994), 933–936.

(35) Pacchioni, G.; Freund, H. *Chem. Rev.* **2013**, *113* (6), 4035–4072.

(36) Metois, J. J.; Heinemann, K.; Poppa, H. *Thin Solid Films* **1977**, *41* (2), 197–207.

(37) Duriez, C.; Chapon, C.; Henry, C. R.; Rickard, J. M. *Surf. Sci.* **1990**, *230*, 123–136.

(38) Stankic, S.; Müller, M.; Diwald, O.; Sterrer, M.; Knözinger, E.; Bernardi, J. *Angew. Chemie Int. Ed.* **2005**, *44* (31), 4917–4920.

(39) Xu, C.; Goodman, D. W. *Chem. Phys. Lett.* **1997**, *265* (3–5), 341–346.

(40) Xu, C.; Oh, W. S.; Liu, G.; Kim, D. Y.; Goodman, D. W. *J. Vac. Sci. Technol. A Vacuum, Surfaces, Film.* **1997**, *15* (1997), 1261–1268.

(41) Gallagher, M. C.; Fyfield, M. S.; Bumm, L. A.; Cowin, J. P.; Joyce, S. A. *Thin Solid Films* **2003**, *445* (1), 90–95.

(42) Wu, M.-C.; Corneille, J. S.; Estrada, C. A.; He, J.-W.; Goodman, D. W. *Chem. Phys. Lett.* **1991**, *182* (5), 472–478.

(43) Perry, S. S.; Kim, H. I.; Imaduddin, S.; Lee, S. M.; Merrill, P. B. *J. Vac. Sci. Technol. A Vacuum, Surfaces, Film.* **1998**, *16* (6), 3402.

(44) Dohnálek, Z.; Kimmel, G. A.; Joyce, S. A.; Ayotte, P.; Smith, R. S.; Kay, B. D. *J. Phys. Chem. B* **2001**, *105* (100), 3747–3751.

(45) Hacquart, R.; Krafft, J. M.; Costentin, G.; Jupille, J. *Surf. Sci.* **2005**, *595* (1–3), 172–182.

(46) Bailly, M. L.; Costentin, G.; Lauron-Pernot, H.; Krafft, J. M.; Che, M. *J. Phys. Chem. B* **2005**, *109* (6), 2404–2413.

(47) Coluccia, S.; Barton, A.; Tench, A. J. *J. Chem. Soc. Faraday Trans. 1 Phys. Chem. Condens. Phases* **1981**, *77* (9), 2203.

(48) Anpo, M.; Yamada, Y.; Kubokawa, Y.; Coluccia, S.; Zecchina, A.; Che, M. *J. Chem. Soc. Faraday Trans. 1 Phys. Chem. Condens. Phases* **1988**, *84* (3), 751.

(49) Benedetti, S.; Benia, H. M.; Nilius, N.; Valeri, S.; Freund, H. J. *Chem. Phys. Lett.* **2006**, *430*, 330–335.

(50) Wichtendahl, R.; Rodriguez-Rodrigo, M.; Härtel, U.; Kuhlenbeck, H.; Freund, H. J. *Surf. Sci.* **1999**, *423* (1), 90–98.

(51) Pacchioni, G. *Surf. Rev. Lett.* **2000**, *7* (3), 277–306.

(52) Pacchioni, G.; Ricart, J. M.; Illas, F. *J. Am. Chem. Soc.* **1994**, *116* (22), 10152–10158.

(53) Zecchina, A.; Stone, F. S. *J. Chem. Soc. Faraday Trans. 1 Phys. Chem. Condens. Phases* **1978**, *74*, 2278.

(54) Scorza, E.; Birkenheuer, U.; Pisani, C. *J. Chem. Phys.* **1997**, *107* (22), 9645.

(55) Wertz, J. E.; Auzins, P.; Weeks, R. A.; Silsbee, R. H. *Phys. Rev.* **1957**, *107* (6), 1535–1537.

(56) Sterrer, M.; Fischbach, E.; Risse, T.; Freund, H.-J. *Phys. Rev. Lett.* **2005**, *94* (18), 186101.

(57) Barcaro, G.; Fortunelli, A. *J. Chem. Theory Comput.* **2005**, *1* (5), 972–985.

(58) Caballero, R.; Quintanar, C.; Köster, A. M.; Khanna, S. N.; Reveles, J. U. *J. Phys. Chem. C* **2008**, *112* (38), 14919–14928.

(59) Molina, L.; Hammer, B. *J. Catal.* **2005**, *233* (2), 399–404.

(60) Yang, Z.; Wu, R.; Zhang, Q.; Goodman, D. W. *Phys. Rev. B - Condens. Matter Mater. Phys.* **2002**, *65* (15), 155407.

(61) Yoon, B.; Häkkinen, H.; Landman, U.; Wörz, A. S.; Antonietti, J.-M.; Abbet, S.; Judai, K.; Heiz, U. *Science* **2005**, *307* (5708), 403–407.

(62) Lin, X.; Yang, B.; Benia, H. M.; Myrach, P.; Yulikov, M.; Aumer, A.; Brown, M. A.; Sterrer, M.; Bondarchuk, O.; Kieseritzky, E.; Rocker, J.; Risse, T.; Gao, H. J.; Nilius, N.; Freund, H. J. *J. Am. Chem. Soc.* **2010**, *132* (22), 7745–7749.

(63) Ricci, D.; Di Valentin, C.; Pacchioni, G.; Sushko, P. V.; Shluger, A. L.; Giamello, E. *J. Am. Chem. Soc.* **2003**, *125* (3), 738–747.

(64) Chiesa, M.; Paganini, M. C.; Giamello, E.; Murphy, D. M.; Di Valentin, C.; Pacchioni, G. *Acc. Chem. Res.* **2006**, *39* (11), 861–867.

(65) Robins, J. L.; Rhodin, T. N. *Surf. Sci.* **1964**, *2*, 346–355.

(66) Kizuka, T.; Tanaka, N. *Phys. Rev. B* **1997**, *56* (16), R10079–R10088.

(67) Brown, M. A.; Fujimori, Y.; Ringleb, F.; Shao, X.; Stavale, F.; Nilius, N.; Sterrer, M.; Freund, H. J. *J. Am. Chem. Soc.* **2011**, *133* (27), 10668–10676.

(68) Brown, M. A.; Carrasco, E.; Sterrer, M.; Freund, H. J. *J. Am. Chem. Soc.* **2010**, *132* (12), 4064–4065.

(69) Hemmingson, S. L.; Campbell, C. T. *ACS Nano* **2016**, Just Accepted Manuscript DOI: 10.1021/acsnano.6b07502.

(70) Sellers, J. R. V.; James, T. E.; Hemmingson, S. L.; Farmer, J. A.; Campbell, C. T. *Rev. Sci. Instrum.* **2013**, *84* (12), 123901.

(71) *CRC Handbook of Chemistry and Physics*, 95th ed.; Hayes, W. M., Ed.; CRC Press: Boston, MA, 2014.

(72) Stuckless, J. T.; Frei, N. A.; Campbell, C. T. *Rev. Sci. Instrum.* **1998**, *69* (6), 2427.

(73) Comsa, G.; David, R. *Surf. Sci. Rep.* **1985**, *5* (4), 145–198.

(74) Pauls, S. W.; Campbell, C. T. *Surf. Sci.* **1990**, *226* (3), 250–256.

(75) Stuckless, J. T.; Frei, N. A.; Campbell, C. T. *Sensors Actuators B Chem.* **2000**, *62* (1), 13–22.

(76) Farmer, J. A.; Baricuatro, J. H.; Campbell, C. T. *J. Phys. Chem. C* **2010**, *114* (40), 17166–17172.

(77) Kim, Y. D.; Stultz, J.; Goodman, D. W. *Surf. Sci.* **2002**, *506* (3), 228–234.

(78) Campbell, C. T.; Starr, D. E. *J. Am. Chem. Soc.* **2002**, *124* (31), 9212–9218.

(79) Sharp, J. C.; Campbell, C. T. *Surf. Sci.* **2015**, *632*, L5–L8.

(80) Campbell, C. T. *Surf. Sci. Rep.* **1997**, *27* (1–3), 1–111.

(81) Venables, J. A.; Spiller, G. D. T.; Hanbucken, M. *Reports Prog. Phys.* **1984**, *47* (4), 399–459.

(82) Venables, J. A. *Surf. Sci.* **1994**, *299–300*, 798–817.

(83) Shigeta, Y.; Maki, K. *Jpn. J. Appl. Phys.* **1979**, *18* (1), 71–78.

(84) Diebold, U.; Pan, J.-M.; Madey, T. E. *Phys. Rev. B - Condens. Matter Mater. Phys.* **1993**, *47* (7), 3868–3876.

(85) Campbell, C. T.; James, T. E. *Surf. Sci.* **2015**, *641*, 166–169.

(86) James, T. E.; Hemmingson, S. L.; Campbell, C. T. *ACS Catal.* **2015**, *5*, 5673–5678.

(87) Starr, D. E.; Campbell, C. T. *J. Phys. Chem. B* **2001**, *105* (18), 3776–3782.

(88) Hemmingson, S. L.; James, T. E.; Feeley, G. M.; Tilson, A. M.; Campbell, C. T. *J. Phys. Chem. C* **2016**, *120* (22), 12113–12124.

(89) James, T. E.; Hemmingson, S. L.; Ito, T.; Campbell, C. T. *J. Phys. Chem. C* **2015**, *119* (30), 17209–17217.

(90) Henry, C. R. *Prog. Surf. Sci.* **2005**, *80* (3–4), 92–116.

(91) Sato, H. *J. Vac. Sci. Technol.* **1969**, *6* (1), 62.

(92) Socha, R. P.; Zackiewicz, E.; Spiridis, N.; Korecki, J. *Surf. Interface Anal.* **2010**, *42* (6–7), 536–539.

(93) Venables, J. A.; Harding, J. H. *J. Cryst. Growth* **2000**, *211* (1), 27–33.

(94) Vitto, A. Del; Pacchioni, G.; Delbecq, F.; Sautet, P. *J. Phys. Chem. B* **2005**, *109* (100), 8040–8048.

(95) Harsdorff, M.; Knabbe, E. A. *Surf. Sci.* **1979**, *86*, 36–41.

(96) Yudanov, I.; Pacchioni, G.; Neyman, K.; Rösch, N. *J. Phys. Chem. B* **1997**, *101* (15), 2786–2792.

(97) Frondelius, P.; Häkkinen, H.; Honkala, K. *Phys. Rev. B - Condens. Matter Mater. Phys.* **2007**, *76* (7), 1–4.

(98) Honkala, K.; Häkkinen, H. *J. Phys. Chem. C* **2007**, *111* (100), 4319–4327.

(99) Sicolo, S.; Giordano, L.; Pacchioni, G. *J. Phys. Chem. C* **2009**, *113* (100), 16694–16701.

(100) Pacchioni, G.; Giordano, L.; Baistrocchi, M. *Phys. Rev. Lett.* **2005**, *94* (22), 226104.

(101) Yulikov, M.; Sterrer, M.; Heyde, M.; Rust, H.-P.; Risse, T.; Freund, H.-J.; Pacchioni, G.; Scagnelli, A. *Phys. Rev. Lett.* **2006**, *96* (14), 146804.

(102) Ernst, K.; Ludviksson, A.; Zhang, R.; Yoshihara, J.; Campbell, C. *Phys. Rev. B* **1993**, *47* (20), 13782–13796.

(103) Ricci, D.; Bongiorno, A.; Pacchioni, G.; Landman, U. *Phys. Rev. Lett.* **2006**, *97* (3), 1–4.

(104) Sterrer, M.; Risse, T.; Heyde, M.; Rust, H. P.; Freund, H. J. *Phys. Rev. Lett.* **2007**, *98* (20), 6–9.

(105) Ranney, J. T.; Starr, D. E.; Musgrove, J. E.; Bald, D. J.; Charles, C. T. *Faraday Discuss.* **2000**, No. 114, 195–208.

(106) Larsen, J.; Ranney, J.; Starr, D.; Musgrove, J.; Campbell, C. T. *Phys. Rev. B* **2001**, *63* (19), 195410.

(107) Metois, J. J.; Heinemann, K.; Poppa, H. *Appl. Phys. Lett.* **1976**, *29* (3), 134–136.

(108) Starr, D.; Ranney, J.; Larsen, J.; Musgrove, J.; Campbell, C. T. *Phys. Rev. Lett.* **2001**, *87* (10), 106102.

(109) Tersoff, J.; Tromp, R. M. *Phys. Rev. Lett.* **1993**, *70* (18), 2782–2785.

(110) Tyson, W. R.; Miller, W. A. *Surf. Sci.* **1977**, *62* (1), 267–276.

(111) Didier, F.; Jupille, J. *Surf. Sci.* **1994**, *307–309*, 587–590.

(112) Kubo, M.; Miura, R.; Yamauchi, R.; Vetrivel, R.; Miyamoto, A. *Appl. Surf. Sci.* **1995**, *89* (2), 131–139.

(113) Giorgio, S.; Cabie, M.; Henry, C. R. *Gold Bull.* **2008**, *41* (2), 167–173.

(114) Kantorovich, L. N.; Holender, J. M.; Gillan, M. J. *Surf. Sci.* **1995**, *343* (3), 221–239.

(115) Pacchioni, G.; Pescarmona, P. *Surf. Sci.* **1998**, *412–413*, 657–671.

(116) Sushko, P. V.; Shluger, A. L.; Catlow, C. R. A. *Surf. Sci.* **2000**, *450* (3), 153–170.

FIGURES

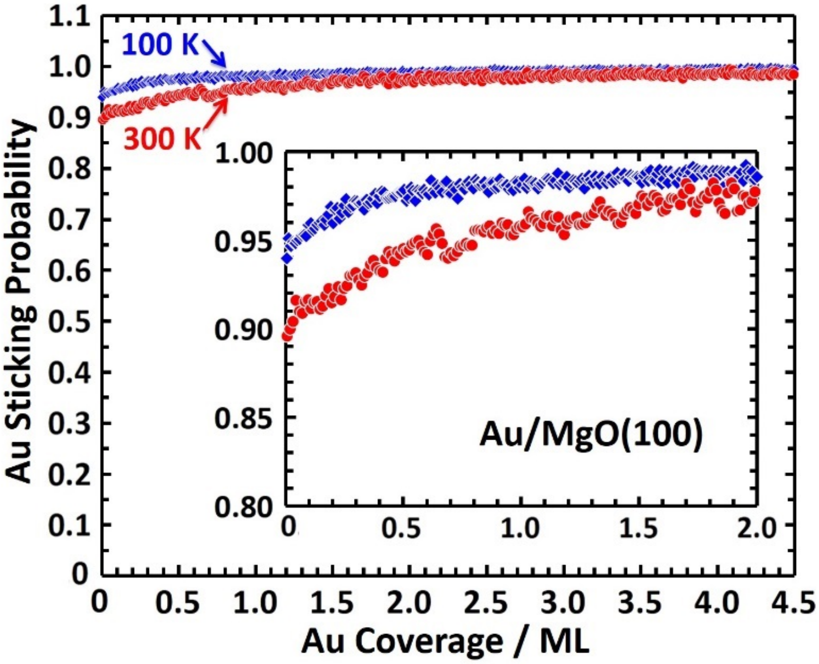

Figure 1: Measured sticking probability of Au atoms on MgO(100) as a function of total Au coverage in ML at 300 K (red circles) and 100 K (blue diamonds). The data at each temperature represent the average of three runs. The sticking probability starts at 90% at 300 K, 95% at 100 K, and reaches unity sticking by ~2 ML at both temperatures.

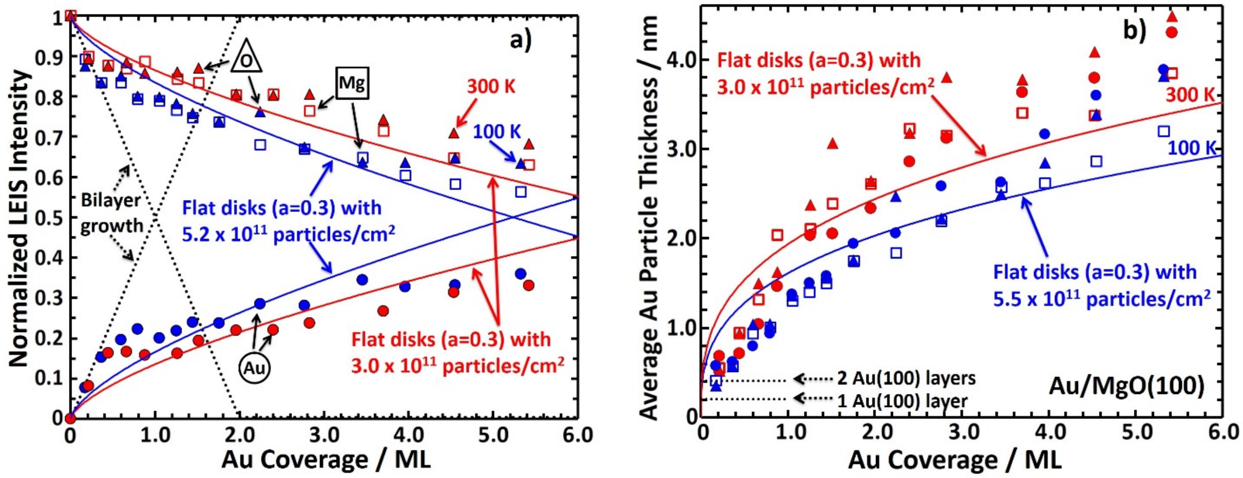

Figure 2: (a) Integrated LEIS signal intensities for Au (closed circles), O (closed triangles), and Mg (open squares) as a function of total Au coverage on MgO(100). Data at both 300 K (red) and 100 K (blue) are shown. The substrate signals are normalized to the clean MgO(100) film, while the Au signals are normalized to the final Au coverage point scaled by the average of the remaining Mg and O signals to represent a thick Au overlayer covering the substrate. For Au coverages of 40-60 ML, ~25% of the Mg and O was typically still visible in LEIS. The black dashed lines correspond to the normalized LEIS signal expected from a bilayer growth mechanism. The solid red (300 K) and blue (100 K) line correspond to Au growing as flat circular disks with a fixed aspect ratio of 0.3 and a fixed particle density that is fit to the data at 2 ML. This particle density that best fits the 2 ML data is 3.0 x 10^{11} particles/cm^2 at 300 K and 5.2 x 10^{11} particles/cm^2 at 100 K. **(b):** Average Au particle thickness versus Au coverage as measured by LEIS assuming flat circular disks with a constant number density determined by fitting Figure 2(a) at 2 ML with the STM-measured aspect ratio, and assuming a constant macroscopic shadowing factor of 1.382. These thicknesses were found using the Au, O, and Mg LEIS data from Figure 2(a) (using the same symbols). The solid curves are the expected result from the same flat-disk, fixed-aspect-ratio model and particle number densities shown in Figure 2(a). Using this representation, the failure of this fixed-aspect-ratio model is clear – Au particles are *thinner* than this model predicts at low coverages and *thicker* at high coverages, i.e., their aspect ratio is constantly increasing with coverage above ~0.3 ML.

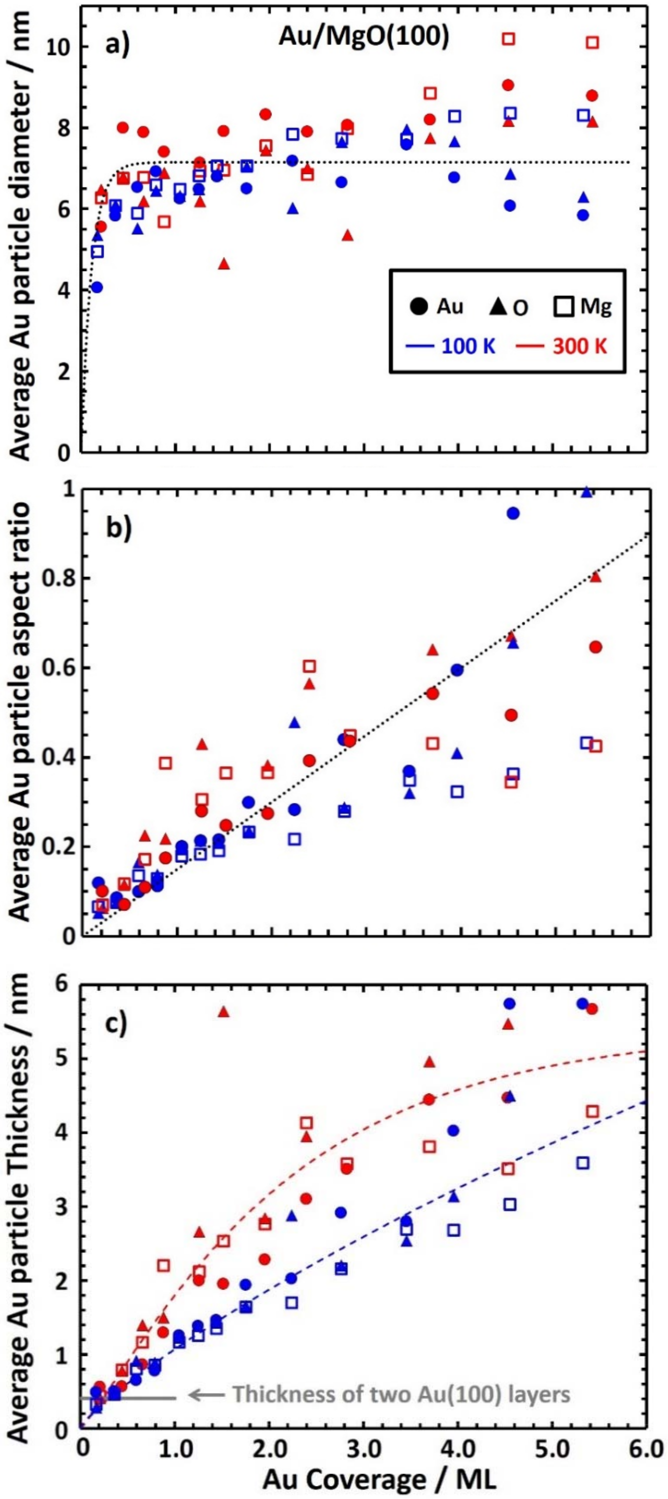

Figure 3: Average Au particle **a)** diameter and **b)** aspect ratio calculated concurrently from the total quantity of Au deposited and the fractional Au coverage as determined by the normalized LEIS signals from Figure 2(a) for Au (closed circles), O (closed triangles), and Mg (open squares) at 300 K (red) and 100 K (blue). These two Au particle parameters were determined

from each LEIS point by assuming that the particle density remains constant at all coverages, and is equal to the best fit values at 2 ML for 300 K and 100 K from Figure 2(a). The black dotted lines are shown to guide the eye, and indicate that Au particles increase rapidly in diameter from 0-0.4 ML, after which they grow thicker but with constant diameter from 0.5-3 ML. The aspect ratio increases nearly linearly with coverage above 0.5 ML at both temperatures. **c)** Real average Au particle thickness determined using the total amount of Au deposited, the aspect ratio, and the diameter at each point, using a macroscopic shadowing factor that is determined by the aspect ratio at each point. Compared to Figure 2(b), the low-coverage points are even thinner and the high-coverage points even thicker than the constant-aspect ratio model predicted. Using a varying aspect ratio reveals that the first several coverage points lie at the thickness of an Au(100) bilayer. The dashed red and blue lines correspond to exponential fits to the 300 K and 100 K data, respectively, to map Au coverage to average particle thickness.

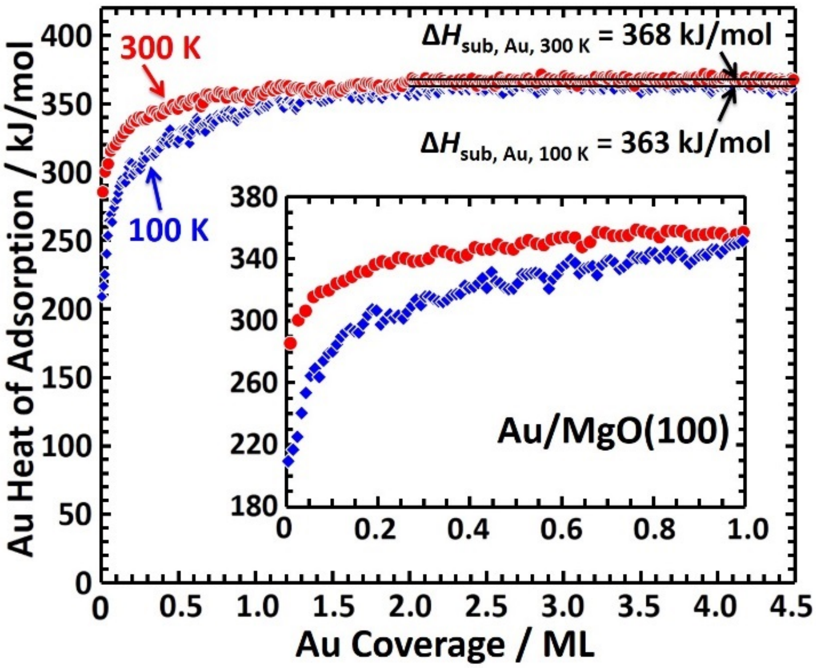

Figure 4: Heats of Au atom adsorption on MgO(100) at 300 K (red circles) and at 100 K (blue diamonds) as a function of total Au coverage (1 ML = 1.12 x 10^{15} atoms/cm^2). The inset expands the range from 0-1 ML where the heat changes most rapidly with coverage.

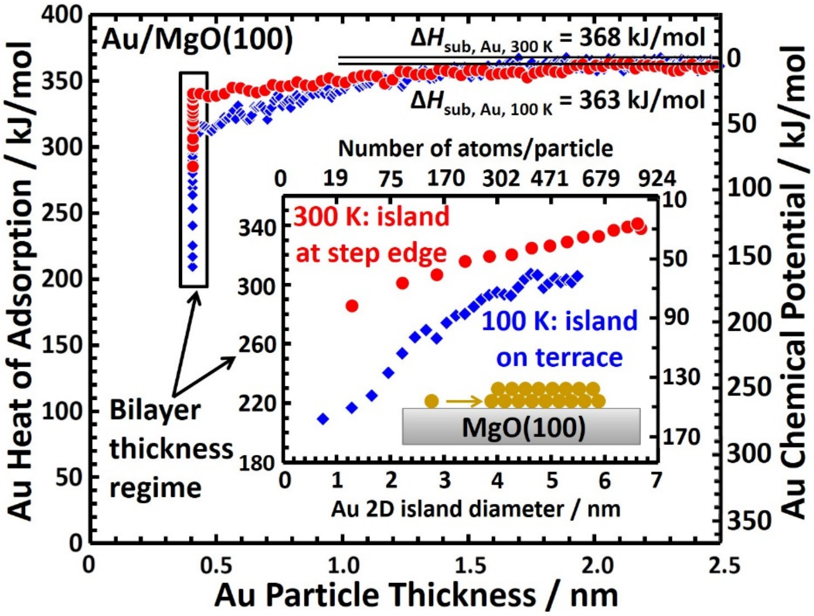

Figure 5: Au heat of adsorption (left axis) and the chemical potential of Au atoms in Au nanoparticles (right axis) versus average Au particle thickness, which is obtained from the total Au coverage using the exponential fits to the data in Figure 4(c). Data that falls below the thickness of one Au(100) bilayer (0.407 nm) is forced to this thickness. This is done rather than forcing data to a single layer thickness due to the LEIS results, however it may be possible that some of these very early data points are in fact from single-layer islands. The inset shows the heat and chemical potential data in this 2D-island region as a function of 2D island diameter (bottom axis), which is obtained from the best-fit particle density found in Figure 2 and assuming bilayer thickness. The top axis of the inset shows the number of atoms per island, which is proportional to the square of the island diameter. The data at thicknesses above this 2D-island range show the effect of particle thickness at constant particle diameter of ~7 nm.

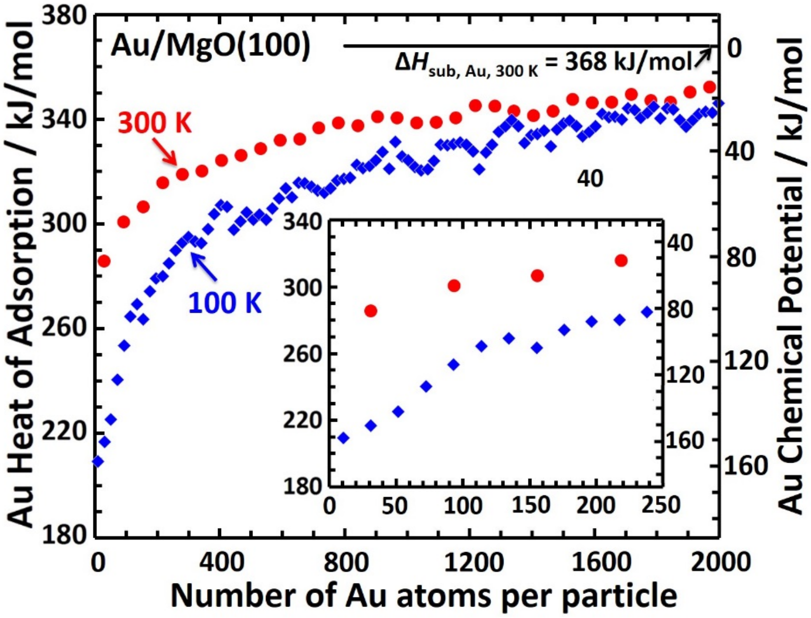

Figure 6: Au heat of adsorption (left axis) and the chemical potential of Au atoms in Au nanoparticles (right axis) at 300 K (red circles) and 100 K (blue diamonds) plotted versus the number of Au atoms per Au particle as determined from the total Au coverage at each point, assuming a constant particle density at the values found in Figure 2 (3.0 x 10^{11} particles/cm^2 at 300 K, 5.2 x 10^{11} particles/cm^2 at 100 K). The smallest number of atoms per particle is 10 for 100 K and 31 for 300 K. The heat data (and therefore chemical potential) for these temperatures are different at similar particle sizes due to the much lower rate of diffusion of Au atoms at 100 K, so that more Au particles occupy the less favorable terrace sites on MgO(100) at 100 K, whereas they grow at the more stable step edges at 300 K. However, as these particles grow larger, the heats converge by the time they reach ~1400 atoms, at which point these particles are large enough that the majority of the heat of adsorption comes from the formation of Au-Au bonds within the particle, with little influence from the bonding to the oxide below.

TOC Image (3.25 x 1.75 inches)